Abl suppresses cell extrusion and intercalation during epithelium folding

Jeanne N. Jodoin and Adam C. Martin*
Department of Biology, Massachusetts Institute of Technology, Cambridge, MA 02142

ABSTRACT **Tissue morphogenesis requires control over cell shape changes and rearrangements. In the *Drosophila* mesoderm, linked epithelial cells apically constrict, without cell extrusion or intercalation, to fold the epithelium into a tube that will then undergo epithelial-to-mesenchymal transition (EMT). Apical constriction drives tissue folding or cell extrusion in different contexts, but the mechanisms that dictate the specific outcomes are poorly understood. Using live imaging, we found that Abelson (Abl) tyrosine kinase depletion causes apically constricting cells to undergo aberrant basal cell extrusion and cell intercalation. *abl* depletion disrupted apical–basal polarity and adherens junction organization in mesoderm cells, suggesting that extruding cells undergo premature EMT. The polarity loss was associated with abnormal basolateral contractile actomyosin and Enabled (Ena) accumulation. Depletion of the Abl effector Enabled (Ena) in *abl*-depleted embryos suppressed the *abl* phenotype, consistent with cell extrusion resulting from misregulated *ena*. Our work provides new insight into how Abl loss and Ena misregulation promote cell extrusion and EMT.**

Monitoring Editor
Denise Montell
University of California, Santa Barbara

Received: May 27, 2016
Revised: Jun 20, 2016
Accepted: Jul 11, 2016

INTRODUCTION

Embryonic development requires morphogenetic events that alter the shape of cells and tissues (Lecuit *et al.*, 2011). Defects in tissue morphogenesis result in abnormal organ formation, and genes and processes that reactivate morphogenetic processes later in life have been linked to metastasis (Yamada and Cukierman, 2007; Wang *et al.*, 2012). Thus it is important to understand how morphogenesis is precisely regulated. Epithelial tissue folding is driven by apical constriction, a cell-shape change that alters a columnar cell into a wedged-shape cell (Leptin and Grunewald, 1990; Leptin, 1995). During constriction, nonmuscle myosin II (MyoII) contracts a network of actin filaments (F-actin) spanning the apical surface, generating a force that is propagated across the tissue via catenin-cadherin–containing adherens junctions (AJs) (Franke *et al.*, 2005; Martin *et al.*, 2009, 2010). In addition, apical constriction drives other morphogenetic events, such as cell extrusion and delamination (Marinari *et al.*, 2012; Slattum and Rosenblatt, 2014), although the mechanism determining the morphogenetic outcome of apical constriction is poorly understood.

In *Drosophila*, transcription factors Twist and Snail promote both apical constriction of ventral cells to induce tissue folding into an epithelial tube within the embryo (called the ventral furrow; Figure 1A) and then epithelial-to-mesenchymal transition (EMT) of the epithelial tube (Leptin, 1991; Martin *et al.*, 2009; Clark *et al.*, 2011). Twist and Snail promote EMT, in part, via repression of E-cadherin (E-cad) transcriptional activation (Vesuna *et al.*, 2008; Shamir *et al.*, 2014). E-cad repression promotes the loss of apical–basal polarity and cell–cell junctions and induces cell migration of the mesoderm, features recapitulated in metastatic cancer (Onder *et al.*, 2008). Reactivation of the EMT program later in life results in this disease state. Apically constricting cells are mechanically coupled to each other during tissue folding (Martin *et al.*, 2010), and no cell extrusion occurs, suggesting that a mechanism functions to prevent cell extrusion before EMT.

Abl tyrosine kinase has conserved roles in tissue morphogenesis and disease states (Koleske *et al.*, 1998; Fox and Peifer, 2007). *Drosophila* Abl regulates apical F-actin organization during apical constriction and tissue folding via negative regulation of Enabled (Ena; Fox and Peifer, 2007). Ena binds to F-actin barbed

This article was published online ahead of print in MBoC in Press (http://www.molbiolcell.org/cgi/doi/10.1091/mbc.E16-05-0336) on July 20, 2016.
The authors declare no competing financial interests.
*Address correspondence to: Adam C. Martin (acmartin@mit.edu).
Abbreviations used: Abl, Abelson; AJ, adherens junction; β-cat, β-catenin; dsRNA, double-stranded RNA; E-cad, E-cadherin; EMT, epithelial-to-mesenchymal transition; Ena, Enabled; MyoII, myosin II; shRNA, small hairpin RNA.

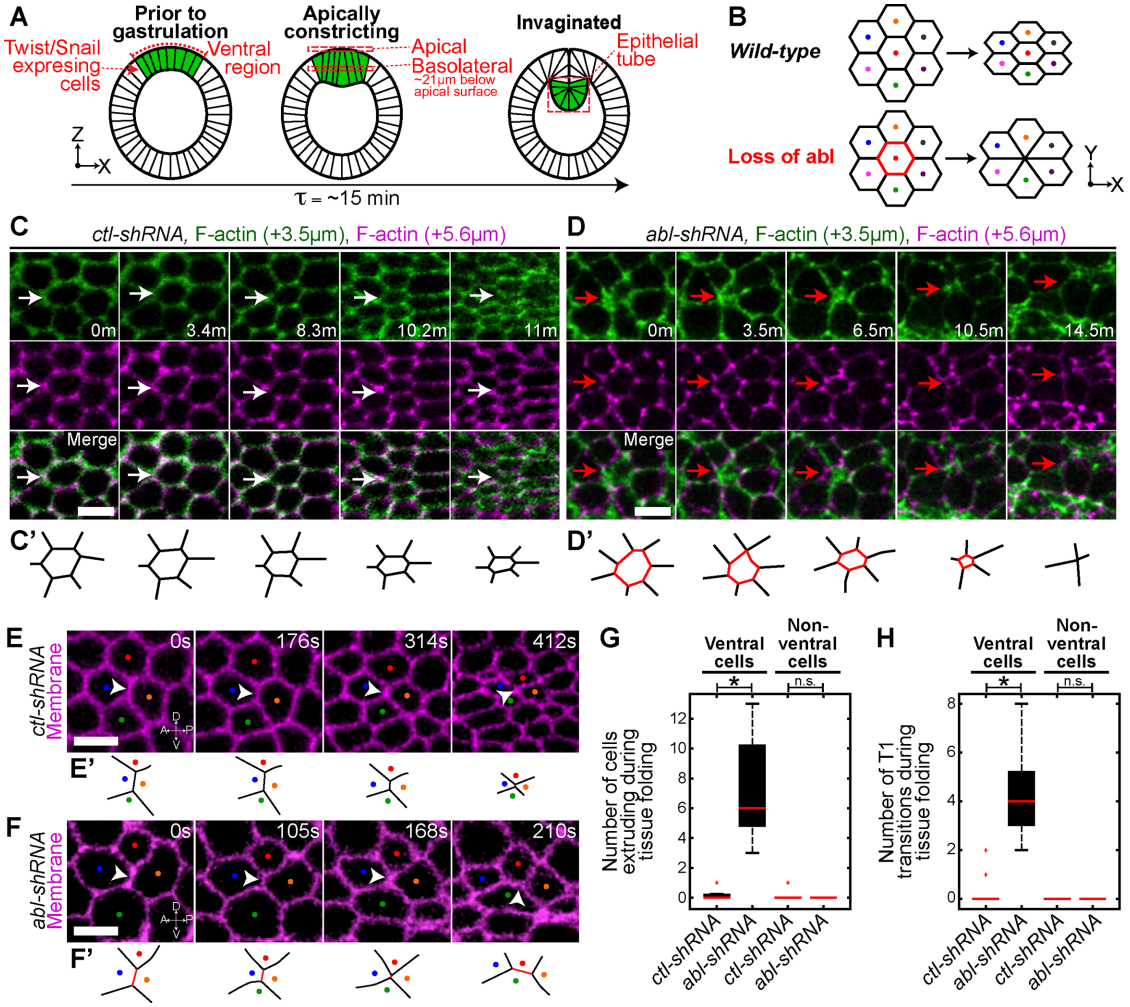

FIGURE 1: Abl suppresses cell extrusion and intercalation during apical constriction. (A) Schematic of ventral furrow formation. Green denotes Twist and Snail expressing–ventral cells. (B) Schematic of cell behavior during apical constriction. Colored dots track cells. Red cell denotes cell extrusion. (C, D) Time-lapse images of constricting cells from embryos expressing indicated UAS-shRNA and Utr::GFP (F-actin, cell outlines) at indicated depths below the apical surface. White arrow denotes a constricting cell. Red arrow denotes basal cell extrusion after loss of *abl*. (C′, D′) Schematized cells denoted by the white and red arrows in C and D, respectively. (E, F) Time-lapse images of embryos expressing indicated UAS-shRNA and Gap43::CH (membrane). White arrowheads and colored dots track an interface and cells, respectively. (E′, F′) Schematized interface denoted by white arrowheads in E and F, respectively. (G) Number of cells extruding during tissue folding. (H) Number of T1 transitions during tissue folding. Box plots (in this and all subsequent figures): red line, median; bottom and top, 25th and 75th percentiles, respectively; black dashed lines, lowest and highest values; red crosses, outliers beyond 1.5 times the interquartile range of the box edges. *$p < 0.00001$. n.s., not significant. Scale bars, 5 µm. See *Materials and Methods* for data point numbers for all experiments in this and all subsequent figures.

ends to promote actin elongation and restrict actin capping (Bear and Gertler, 2009; Hansen and Mullins, 2010). Abl also promotes AJ dynamics during tissue elongation via β-catenin (β-cat; *Drosophila armadillo*) phosphorylation (Tamada *et al.*, 2012). In mammalian systems, misregulation of Abl is associated with metastasis; Abl overexpression leads to hyperproliferation and tumor formation, and Abl depletion results in metastasis and invasion (Hayes *et al.*, 2013). Moreover, increased levels of mammalian Ena increase the occurrence of metastasis in animal models and breast cancer (Philippar *et al.*, 2008; Oudin *et al.*, 2016). Here we identify a mechanism by which loss of Abl and Ena misregulation, combined with Snail and Twist expression, promotes EMT-like behavior during tissue folding.

RESULTS

Abl prevents cell extrusion and intercalation of ventral cells during apical constriction

During *Drosophila* gastrulation, ventral cells apically constrict in a coordinated manner; cells constrict their apical surface at similar rates, such that apical surface areas are homogeneous (Figure 1, A and B). Abl is required for this coordinated apical constriction; abl^4-null mutants exhibited uncoordinated constriction, resulting in populations of larger, unconstricted cells (Supplemental Figure S1B, green arrow) and smaller, constricted cells (Supplemental Figure S1B, red arrow; Fox and Peifer, 2007). Flies expressing small hairpin RNA (shRNA) targeting *abl*, which effectively depletes ~83% of *abl* transcript (Jodoin *et al.*, 2015), recapitulated the uncoordinated-constriction

phenotype (Supplemental Figure S1A), confirming that this is an effective tool with which to study Abl during tissue folding.

We previously performed a live-imaging RNA interference screen targeting known actomyosin regulators (Jodoin *et al.*, 2015) and identified a surprising and unreported phenotype in *abl-shRNA* embryos. Live imaging of *abl*-depleted embryos revealed that ventral cells frequently undergo basal cell extrusion during tissue folding, a phenotype not observed in *wild-type* or control embryos (Figure 1, B–D, and G, Supplemental Figure S1, E, F, J, and K, and Supplemental Movie S1). Extrusion was not observed in cells adjacent to the ventral region that do not express Twist and Snail (nonventral cells; Figure 1G). This suggests that Abl promotes the maintenance of cells within the epithelium during tissue folding. Loss of *abl* results in a disorganized, apical actomyosin meshwork, with some cells lacking apical actomyosin (Fox and Peifer, 2007). However, apical actomyosin pulses were observed in extruding cells (Supplemental Figure S1H; 17 of 17 embryos). Nuclei of extruding cells were not fragmented, suggesting that extrusion is not due to an apoptotic signal (Supplemental Figure S1K). Moreover, before the onset of tissue folding, embryos depleted for *abl* exhibit reduced cell packing (*ctl-shRNA*, 24 ± 1.1, and *abl-shRNA*, 19.9 ± 0.74, cells per 35-μm^2 area; $p < 0.00001$), suggesting that cell extrusion is not due to cell crowding. In addition to extrusion, intercalation events known as T1 transitions, in which junctions aligned along the dorsal–ventral axis collapse and extend new junctions along the anterior–posterior axis (Bertet *et al.*, 2004), were observed specifically in ventral cells during tissue folding in *abl*-depleted embryos (Figure 1, F and H, and Supplemental Figure S1G). T1 transitions were not observed in control embryos during tissue folding in either ventral or nonventral cells because this is before tissue elongation (Figure 1, E and H, and Supplemental Figure S1G). Aberrant ventral region T1 transitions occur with preferred direction, with junctions oriented along the dorsal–ventral axis shrinking and junctions along the anterior–posterior axis lengthening despite a lack of planar polarized actomyosin, which is important for intercalation during tissue elongation (Bertet *et al.*, 2004; Zallen and Wieschaus, 2004). The elongation is in the direction in which tension is normally highest in the ventral furrow (Martin *et al.*, 2010), suggesting that intercalation may be a response to global tissue tension. Together these data suggest that *abl* functions to prevent cell extrusion and intercalation specifically in Twist- and Snail-expressing cells during tissue folding.

Abl regulates apical–basal polarity of ventral cells

After tissue folding and tube formation, ventral cells lose apical–basal polarity and undergo EMT (Clark *et al.*, 2011). To determine whether cell extrusion is due to early EMT-like behavior, we tested whether *abl* depletion altered apical–basal polarity. During apical constriction, the cell polarity protein Par-3 (*Drosophila Bazooka*) localizes apically and establishes the apical domain by setting the position of AJs (Figure 2D, ctl-shRNA, yellow arrows; Harris and Peifer, 2004, 2005). *abl* depletion resulted in the basolateral accumulation of Par-3 specific to the ventral region (Figure 1A, apically constricting; Figure 2, B–E, red arrows, and Supplemental Figure S1I). This accumulation below that apical surface due to the loss of *abl* occurred after the onset of tissue folding (Figure 2C, red arrows). In contrast, Par-3 is restricted apically and not present in the basolateral domain of *ctl-shRNA* embryos (Figure 2, A, and C–E, yellow arrows). These data suggest that *abl* maintains apical–basal polarity in ventral cells during tissue folding.

Apical and basolateral E-cad organization of ventral cells requires *abl*

Apical AJs are essential for segregating apical and basolateral cues (Harris and Peifer, 2004). A reduction of AJ components in apically constricting cells results in a loss of apical identity (Harris and Peifer, 2004) and aberrant T1 transitions (Martin *et al.*, 2010). Thus we next assessed whether loss of *abl* disrupts apical AJs. In fixed images, E-cad is enriched at apical junctions in a punctate pattern, with relatively low enrichment in the center of the apical surface or the medioapical domain (Figure 2, F, I, and J, *ctl-shRNA*; and Supplemental Figure S1I). In contrast, *abl* depletion resulted in a ventral cell–specific defect in which E-cad was localized across the entire apical surface (Figure 2, F, I, and J, *abl-shRNA*). Live imaging revealed that junctional E-cad observed in *ctl-shRNA* embryos was greatly decreased in *abl-shRNA* embryos, and E-cad became more diffusely localized (Figure 2, K and L). We also observed a striking defect in basolateral E-cad organization after loss of *abl*. In *ctl-shRNA* embryos E-cad is distributed along basolateral junctions, with little variability in its intensity (Figure 2, G and H). Loss of *abl* significantly increased variability in E-cad intensity (Figure 2H), with junctions displaying either a reduction in E-cad levels (Figure 2G, white arrow) or an overaccumulation of E-cad levels (Figure 2G, white arrowhead). Basolateral E-cad levels corresponded to varied basolateral F-actin levels (Figure 2G). Taken together, these data suggest that *abl* promotes proper intercellular junction organization both apically and basolaterally.

Failure to restrict E-cad to cell–cell interfaces and maintain a uniform basolateral organization are likely due to the loss of apical–basal polarity in *abl*-depleted embryos. Basal cell extrusion from an epithelium is often associated with a change in E-cad levels and distribution (Friedl and Wolf, 2003; Slattum and Rosenblatt, 2014). Thus we propose that E-cad defects could play a role in promoting cell extrusion and rearrangements. In other mutants, such as *diaphanous* mutants, E-cad localization is similarly disrupted, but such mutants do not result in cell extrusion (Mason *et al.*, 2013), suggesting that defects in E-cad localization alone are not sufficient to drive extrusion.

Abl restricts actomyosin pulsing to the apical domain in constricting cells

Pulses of contractile actomyosin that drive apical constriction are restricted to the apical domain during tissue folding (Mason *et al.*, 2013). Increased basolateral contractility can drive cell extrusion from the epithelium (Slattum and Rosenblatt, 2014; Wu *et al.*, 2014, 2015). Because we found that Abl promotes apical–basal polarity, we sought to determine whether the apical contractile machinery is localized improperly in *abl-shRNA* embryos. In control embryos, pulsed actomyosin is not present in the basolateral domain (Figure 3, A, C, E, G, and H, *ctl-shRNA*, yellow arrow; and Supplemental Figure S1C). *abl* depletion disrupted the position of contractile actomyosin. Dynamic F-actin, MyoII, and the MyoII activator Rho kinase (ROCK) accumulated basolaterally in *abl*-depleted embryos (Figure 3 B, D, and F–J, *abl-shRNA*, red arrows; and Supplemental Figure S1D, red arrows), suggesting that actomyosin contractility occurs below the apical surface. Basally extruding cells exhibited basolateral pulsed actomyosin, although the presence of basolateral actomyosin in cells did not always result in extrusion (17 of 17 embryos). Moreover, basolateral MyoII and ROCK accumulation occurred at the onset of tissue folding (Figure 3, G and H, red arrows, and Supplemental Movie S2), indicating that the phenotype is not due to delayed folding after loss of *abl* (Figure 3K). On the basis of these findings, we propose that the loss of *abl*

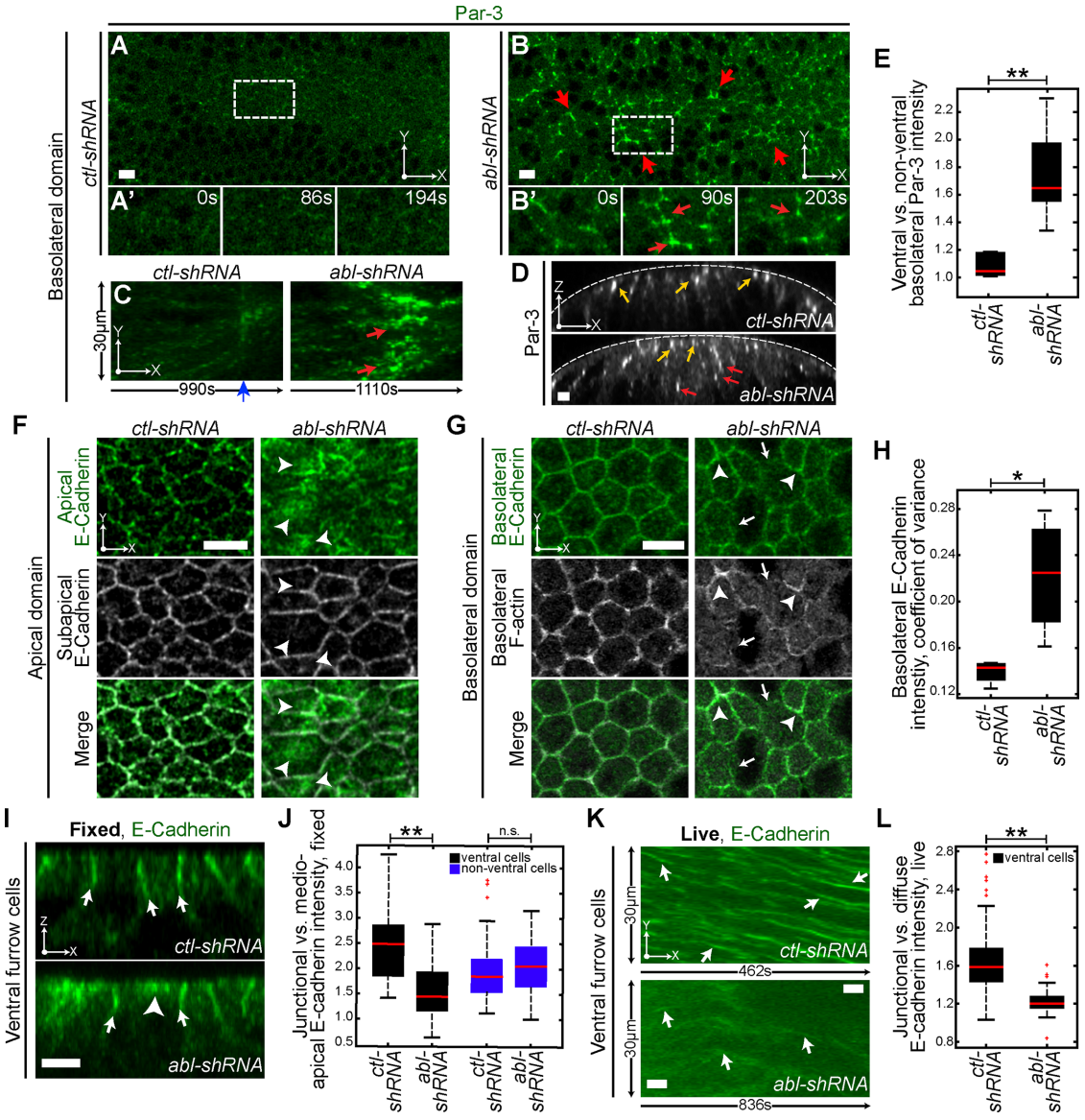

FIGURE 2: Abl depletion disrupts apical–basal polarity in ventral cells. (A–D) Embryos expressing indicated UAS-shRNA and GFP::Bazooka (Par-3). (A, B) Time-lapse images of basolateral domain of ventral cells (~21 µm below the apical surface). Red arrows denote basolateral Par-3. (A′, B′) Zoomed-in region indicated by the white-dashed boxes in A and B, respectively. Red arrows denote dynamic basolateral Par-3. (C) Kymographs of embryos expressing indicated UAS-shRNA and Par-3. Kymographs of basolateral line along the anteroposterior axis. Red arrows denote basolateral Par-3, and blue arrowhead indicates the beginning of tissue folding. (D) Cross-sections. Yellow arrows denote apical Par-3, and red arrows denote basolateral Par-3. (E) Ratio of ventral vs. nonventral basolateral Par-3 intensity. (F) Fixed images of the apical domain in embryos expressing the indicated UAS-shRNA stained for E-cad. Apical E-cad, AJs (green). Subapical E-cad, cell outline (gray). White arrowheads denote pools of medioapical E-cad. (G) Fixed images of the basolateral domain (~21 µm below the apical surface) in embryos expressing the indicated UAS-shRNA and stained for E-cad and phalloidin (F-actin). White arrows denote junctions lacking E-cad, and white arrowheads denote junctions overaccumulated with E-cad. (H) Basolateral E-cad intensity, coefficient of variance. (I) Cross-sections of fixed embryos expressing the indicated UAS-shRNA stained for E-cad. White arrows denote junctional pools of E-cad, and white arrowhead denotes medioapical pool of E-cad. (J) Ratio of junctional vs. medioapical E-cad intensity in fixed embryos. (K) Kymographs of embryos expressing the indicated UAS-shRNA and GFP::Ecad (E-cad). Kymographs are of basolateral line along the anteroposterior axis. Images are maximum intensity projections of the top eight slices of each embryo (~8 µm below apical surface). White arrows denote junctional E-cad. (L) Ratio of junctional vs. diffuse E-cad intensity in live embryos. $^{**}p < 0.00001$, $^{*}p < 0.04$, n.s., not significant. Scale bars, 5 µm.

alters contractility in Twist- and Snail-expressing cells, such that force generation occurs basolaterally in addition to apically (Supplemental Figure S1H), which, coupled with AJ defects, leads to cell extrusion and rearrangements.

Defects in AJ integrity result in basolateral MyoII accumulation

To test whether disrupted apical–basal polarity and AJs could cause actomyosin mislocalization, we mildly reduced β-cat levels via

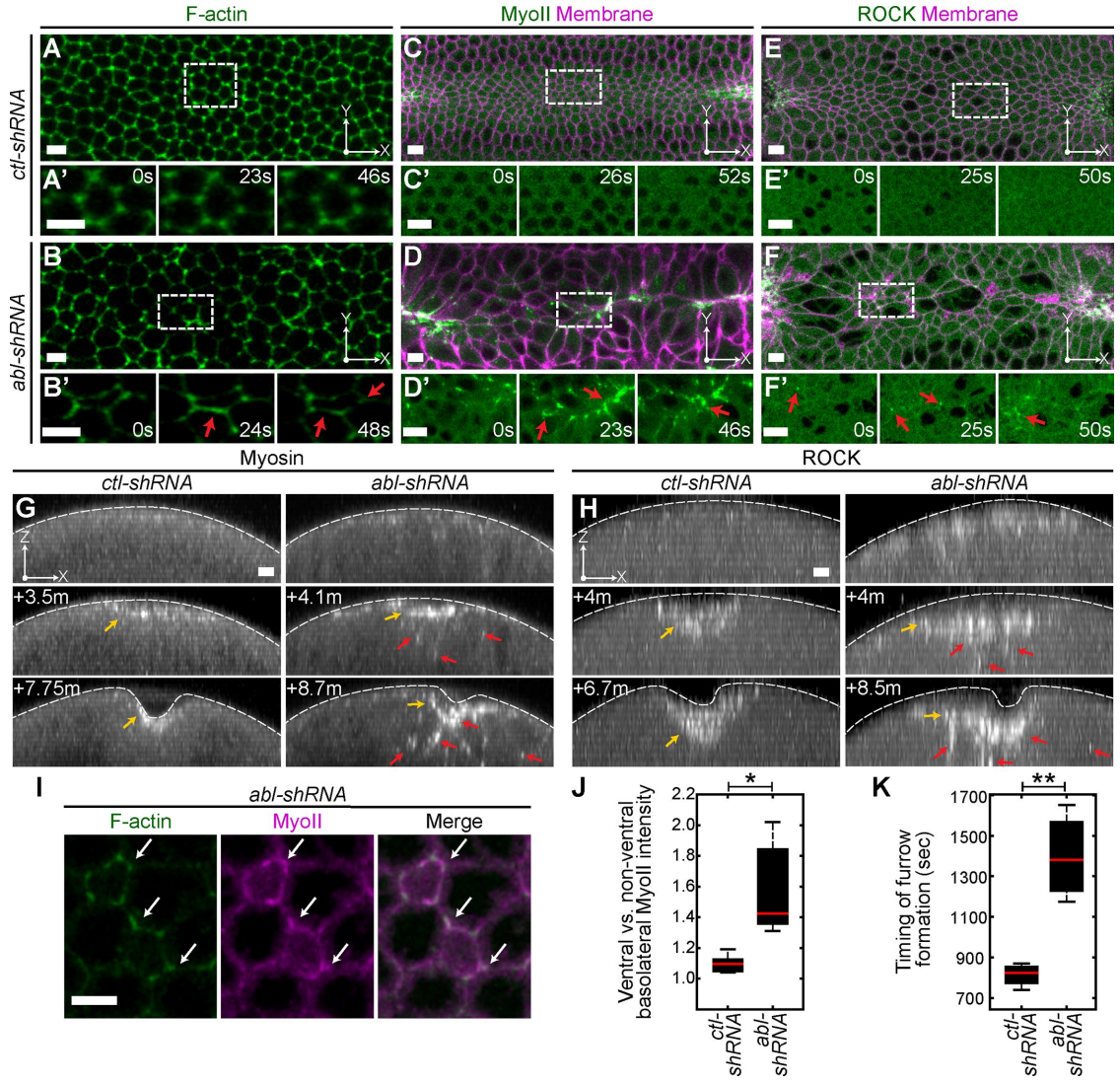

FIGURE 3: Abl depletion causes basolateral actomyosin dynamics in ventral cells. (A–F) Time-lapse images of the basolateral domain (~21 µm below the apical surface) in ventral cells from embryos expressing the indicated UAS-shRNA and Utr::GFP (A, B, F-actin), Sqh::GFP and Gap43::mCherry fluorescent protein (CHFP) (C, D, MyoII and membrane), or ROCK::GFP and Gap43::CHFP (E, F, ROCK and membrane). (A′–F′) Time-lapse images of regions denoted by the white-dashed boxes in A–F, respectively. Red arrow denotes dynamic F-actin (B′), MyoII (D′), or ROCK (F′). (G, H) Time-lapse cross-sections of embryos expressing the indicated UAS-shRNA and Sqh::GFP (G) or ROCK::GFP (H) during apical constriction. Yellow and red arrows denote apical and basolateral pools of MyoII (G) and ROCK (H), respectively. (I) Basolateral domain (~21 µm below the apical surface) in ventral cells from an embryo expressing *abl-shRNA*, F-actin, and Sqh::CHFP (MyoII). White arrows denote basolateral F-actin and MyoII colocalization. (J) Ventral vs. nonventral basolateral MyoII intensity. (K) Timing of furrow formation. $^{**}p < 0.003$, $^{*}p < 0.04$. Scale bars, 5 µm.

injection of β-*cat double-stranded RNA* (*dsRNA*), previously shown to effectively deplete β-*cat* (Tamada *et al.*, 2012), into the embryo. Abl depletion causes partial disruption in AJ organization (Figure 2, F and G). Thus we mildly disrupted AJs to mimic *abl-shRNA* embryos. Complete down-regulation of β-*cat* results in a dramatic separation of ventral cells at the onset of apical constriction (Martin *et al.*, 2010), whereas mild β-*cat* depletion resulted in only slight separations at the poles during the initiation of tissue folding (Supplemental Figure S2A, white arrow). Mild β-*cat* reduction also resulted in aberrant T1 transitions (Supplemental Figure S2D), recapitulating previous reports (Martin *et al.*, 2010) and indicating that AJ integrity is disrupted. In ventral cells, we observed increased basolateral MyoII after mild β-*cat* depletion compared with buffer-only (Ctl) injection (Supplemental Figure S2, B and C, *wild-type* + β-*cat dsRNA*, red arrow), suggesting that the accumulation of basolateral actomyosin in *abl-shRNA* embryos was a downstream consequence of defective AJs. Of importance, basal cell extrusion was not observed in mildly β-*cat*-depleted embryos (Supplemental Figure S2E), suggesting that defects in AJ integrity and basolateral MyoII were not sufficient to induce extrusion. Thus an additional mechanism might be required.

Abl restricts Ena from the basolateral cortex in ventral cells

Ena was identified as an essential effector of *abl* during tissue folding (Fox and Peifer, 2007). In *wild-type* and control embryos, Ena localized diffusely in the cytoplasm (Figure 4, A and E) but became

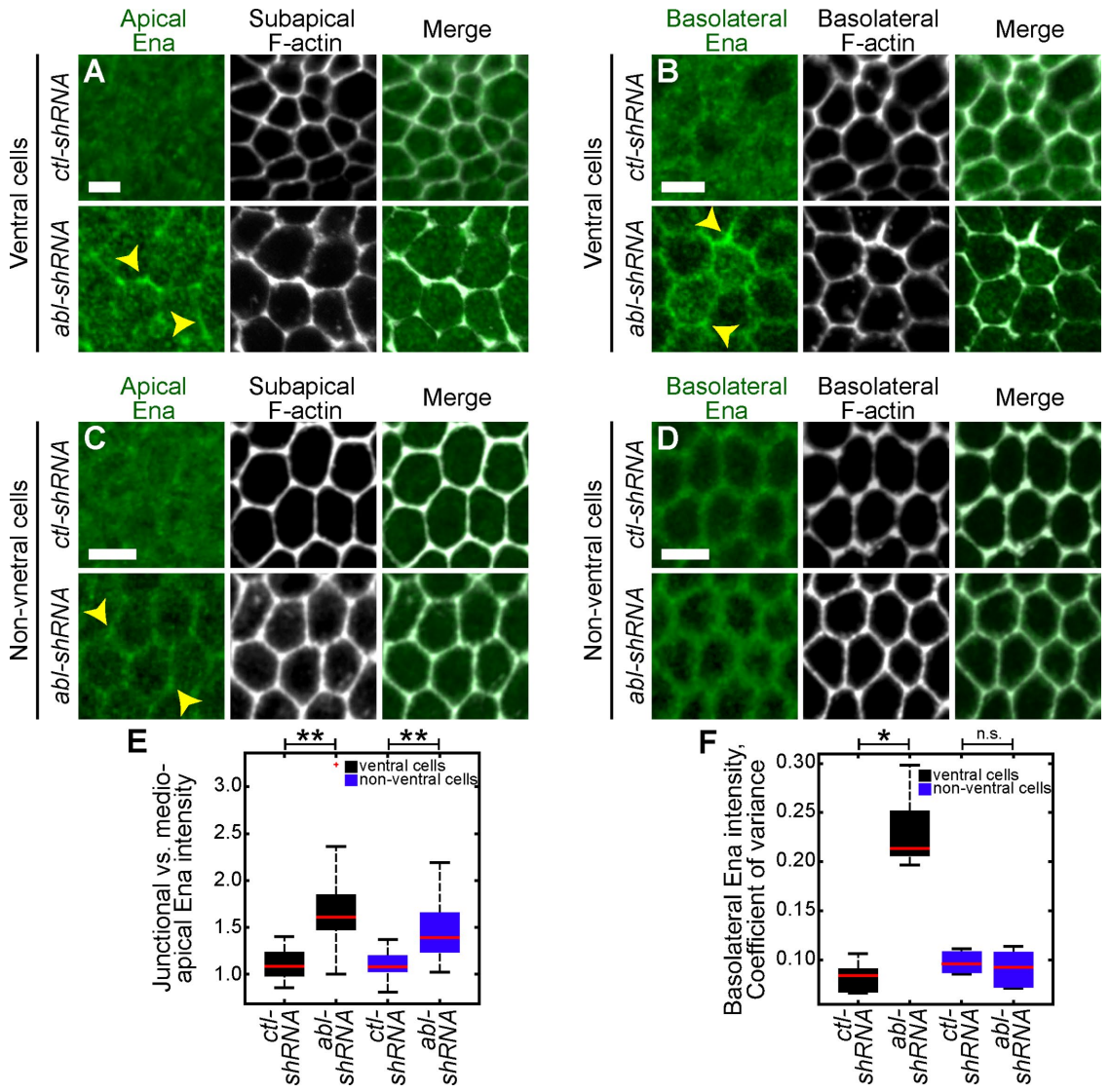

FIGURE 4: *abl* inhibits basolateral, cortical Ena localization in ventral cells. (A–D) Fixed embryos expressing the indicated UAS-shRNA stained for Ena (green) and phalloidin (F-actin, gray) showing either ventral cells (A, B) or nonventral, lateral cells (C, D). Yellow arrowheads denote Ena accumulation at junction. (E) Apical junctional vs. medioapical Ena intensity. (F) Basolateral Ena intensity, coefficient of variance. $^{**}p < 0.00001$, $^{*}p < 0.003$, n.s., not significant. Scale bars, 5 μm.

enriched at intercellular junctions in *abl* mutants (Figure 4, A and E, yellow arrowhead; Fox and Peifer, 2007). We observed that apical Ena was not present uniformly at junctions in *abl-shRNA* embryos, similar to apical E-cad localization (Figures 2F and 4A, yellow arrowhead). In addition, Ena accumulated basolaterally in ventral cells with a localization similar to Par-3 and E-cad after *abl* depletion (Figure 2, B and G, and Figure 4, B and F, yellow arrowhead). Furthermore, basolateral Ena accumulation at junctions was not observed in nonventral cells, although Ena localized to apical junctions in these cells (Figure 4, C–F). This is consistent with the basolateral mislocalization of Ena being specific to Twist- and Snail-expressing cells in the ventral region but not apical Ena accumulation. Ectopic Ena expression locally increases contractility (Furman *et al.*, 2007). On the basis of these data, we hypothesized that the accumulation of basolateral Ena contributes to the cell extrusion present in *abl*-depleted embryos by increasing basolateral contractility.

ena depletion suppresses cell extrusion and rearrangements in an *abl* mutant

To test whether misregulated Ena contributed to cell extrusions and intercalation that occurred in *abl*-depleted embryos, we down-regulated *ena* via injection of *ena-dsRNA*, previously shown to effectively deplete *ena* (Kiger *et al.*, 2003), in *abl-shRNA* embryos. We found that the timing of ventral furrow formation was reduced significantly in *abl,ena*–depleted embryos compared with *abl*-depleted embryos (Figure 5C), showing that dsRNA-mediated depletion of *ena* in *abl-shRNA* embryos suppressed gross tissue-folding defects (Fox and Peifer, 2007). of importance, reducing *ena* levels in *abl-shRNA* embryos suppressed basal cell extrusion and T1 transitions in ventral cells, as well as ventral cell–specific Par-3 and AJ defects (Figure 5, E–H). The ratio of junctional to medioapical E-cad levels increased significantly after *ena-dsRNA* injection compared with Ctl injection, indicating restoration of normal junctional enrichment (Figure 5F). Apical actomyosin meshwork defects and localization

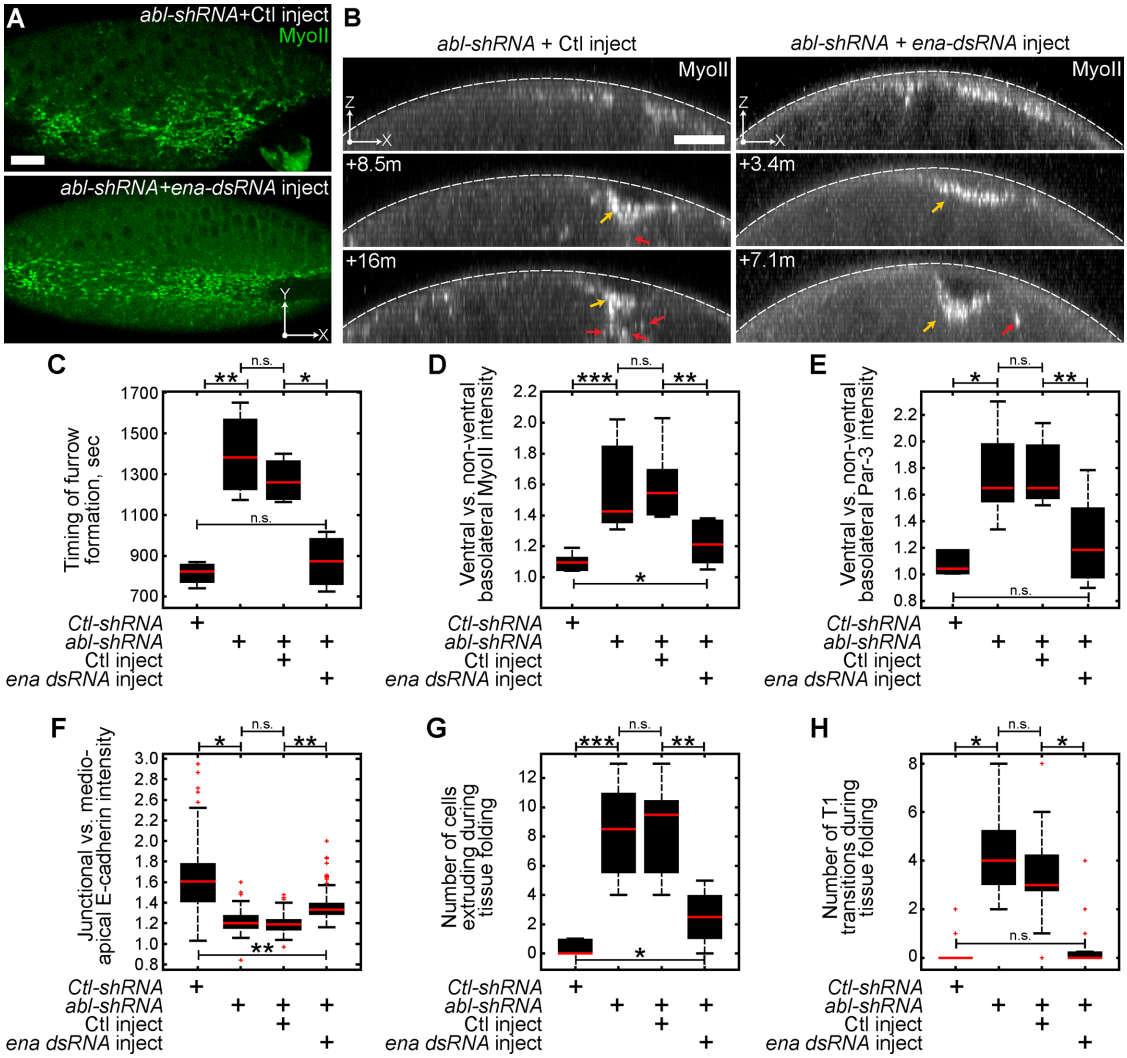

FIGURE 5: Ena depletion suppresses cell extrusion in *abl-shRNA* embryos. (A, B) Embryos expressing *abl-shRNA* and Sqh::GFP (MyoII) after Ctl (buffer only) injection or *ena-dsRNA* injection. (B) Time-lapse cross-sections of embryos expressing *abl-shRNA* and MyoII after the indicated injection. Yellow arrow denotes apical MyoII accumulation. Red arrows denote basolateral MyoII accumulation. (C) Timing of furrow formation. $^{**}p < 0.002$, $^{*}p < 0.006$. (D) Ventral vs. nonventral basolateral MyoII intensity. $^{***}p < 0.003$, $^{**}p < 0.006$, $^{*}p < 0.02$. (E) Ventral vs. nonventral basolateral Par-3 intensity. (F) Junctional vs. medioapical E-cad intensity. $^{**}p < 0.00001$, $^{*}p < 0.0001$. (G) Number of cells extruding during tissue folding. $^{***}p < 0.00001$, $^{**}p < 0.003$, $^{*}p < 0.005$. (H) Number of T1 transitions during tissue folding. $^{*}p < 0.00001$. n.s., not significant. Scale bars, 10 μm.

also were suppressed after *ena-dsRNA* injection. *abl*-depleted embryos displayed a discontinuous apical MyoII meshwork (Figure 5A; Fox and Peifer, 2007), whereas *ena*,*abl*–depleted embryos resulted in a more continuous apical MyoII meshwork (Figure 5A). Moreover, *ena* down-regulation in *abl-shRNA* embryos significantly reduced basolateral accumulation of MyoII (Figure 5, B and D, red arrow). Taken together, these data show that Ena misregulation in *abl*-depleted embryos disrupted apical–basal polarity, AJ positioning, and increased basolateral actomyosin, resulting in basal cell extrusion and intercalation during tissue folding.

DISCUSSION

Previous work described the role of Abl in promoting proper coordinated constriction and apical actomyosin organization during tissue folding (Fox and Peifer, 2007). *abl*-null mutants exhibit populations of both unconstricted and constricted cells and defects in tissue invagination and display discontinuous apical MyoII and F-actin meshworks across the ventral region of the embryo (Fox and Peifer, 2007). Reduction of the Abl effector *ena* in *abl* mutants suppressed gross morphological defects in tissue folding (Fox and Peifer, 2007). Here our work identifies different roles for Abl in maintaining cells within the epithelium during tissue folding, as well as in promoting apical–basal polarity and apical AJ positioning. We found that loss of *abl* results in aberrant basal cell extrusion and cell intercalation events. Correlation between basal cell extrusion and T1 transitions was not observed after loss of *abl*. We found that T1 transitions do not preferentially occur near or after extrusion of a cell or vice versa. Loss of adhesion results in T1 transitions (Supplemental Figure S2D), which occur independently of basal cell extrusion (Supplemental Figure S2E). Together these results suggest that cell extrusion and intercalation are two different outcomes that occur due to the loss of *abl*. Moreover, *abl*-depleted embryos exhibit loss of polarity and AJ organization (Figure 6A), hallmarks of EMT. Because cell extrusion happens specifically in Twist- and Snail-expressing cells, we suggest

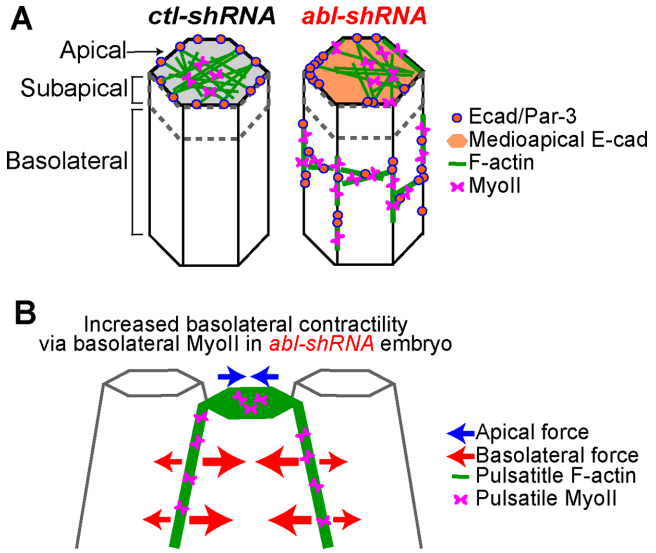

FIGURE 6: Model for basal cell extrusion in *abl-shRNA* embryos. (A) Schematic of ventral cells in *ctl-shRNA* and *abl-shRNA* embryos. (B) Model for how Abl prevents cell extrusion during tissue folding.

that loss of *abl* promotes premature initiation of EMT during the tissue folding process.

Loss of *abl* and cell extrusion are accompanied by relocalization of the apical contractile machinery to basolateral junctions, suggesting that contractility occurs abnormally below the apical surface (Figure 6A), which can drive basal cell extrusion (Wu *et al.*, 2014, 2015). Ena, which can locally increase contractility (Furman *et al.*, 2007), also accumulates along basolateral junctions in *abl* mutants (Figure 6A), further suggesting that the loss of *abl* promotes basolateral contractility. We hypothesize that basolateral contractility, which, in combination with apical contractility, drives basal cell extrusion after loss of *abl* (Figure 6B; Wu *et al.*, 2014, 2015). The heterogeneous nature of Ena and actomyosin accumulation along basolateral junctions could result in random cell extrusion within the ventral region rather than premature EMT of all ventral cells. Understanding why loss of polarity and E-cad organization defects, as well as basolateral actomyosin and Ena accumulation, is not ubiquitous across the ventral region will be important for understanding which cells undergo extrusion and premature EMT. Cells exhibit heterogeneity in their behavior at the onset of apical constriction (Xie and Martin, 2015). This could also play a role in determining which cells undergo extrusion in abl mutants.

Because we did not observe clear correlation between local basolateral actomyosin accumulations and cell extrusion, we suggest that extrusion could result from a nonautonomous effect of basolateral contractility, which could possibly increase lateral pressure on cells in the epithelial sheet. Alternatively, E-cad localized along lateral junctions can organize actin to generate tension; changes in lateral E-cad levels and altered tension are associated with cell extrusion (Wu *et al.*, 2014). Thus changes in E-cad organization along basolateral junctions in *abl* mutants could potentially alter basolateral tension, promoting extrusion. More work is needed to understand the mechanical differences that result in cells and tissues lacking *abl* function. In addition, changes in E-cad organization after loss of *abl* could also play a role in driving basal cell extrusion. Loss of E-cad protein levels is sometimes associated with EMT (Onder *et al.*, 2008). Defects in E-cad organization in *abl-shRNA* embryos could be due to a loss of E-cad protein, thus triggering premature EMT during tissue folding. Altered E-cad localization, namely higher levels of apical E-cad, could also support extrusion by allowing the apical surface to make contact with neighboring cells. Finally, a reduction in basolateral stiffness can lead to cell extrusion (Slattum and Rosenblatt, 2014). Pulsatile actomyosin along basolateral junctions could potentially result in more-rapid F-actin turnover along junctions, as shown in cultured mammalian cells (Wu *et al.*, 2014), reducing the junctional stiffness and promoting cell extrusion. Further work is needed to test these potential models and determine the mechanics driving basal cell extrusion before EMT after the loss of *abl*.

We show here that depletion of *ena* in *abl-shRNA* embryos suppressed all of the observed phenotypes in *abl*-depleted embryos, suggesting that Abl negatively regulates Ena in order to promote epithelial maintenance, polarity, and AJ positioning during tissue folding. During tissue elongation, β-cat was found to be an essential Abl substrate (Tamada *et al.*, 2012); however, because *ena* downregulation suppresses all observed phenotypes (Figure 5), we hypothesize that Ena is the critical Abl effector during tissue folding. Abl is required to inhibit cell intercalation during tissue folding (Figure 1) but functions to promote intercalation during elongation (Tamada *et al.*, 2012). This difference could be due to the expression of Twist and Snail or a difference in the organization of the contractile machinery between tissue folding and elongation. Moreover, loss of *abl* disrupts Par-3 and actomyosin apical–basal polarity during tissue folding (Figures 2 and 3) but not during elongation (Tamada *et al.*, 2012).

Our findings are consistent with those of Fox and Peifer (2007). However, our data show how Abl and Ena regulate an EMT-like process, which provides insight into how Abl and Ena may influence metastasis (Philippar *et al.*, 2008; Hayes *et al.*, 2013; Oudin *et al.*, 2016). Our work highlights the importance of proper Ena regulation via Abl in maintaining cells within the epithelium during tissue folding, before EMT. Kinase-dependent and -independent roles have been identified for Abl in regulating F-actin–dependent processes (Henkemeyer *et al.*, 1990; Dudek *et al.*, 2010; Courtemanche *et al.*, 2015). Whether Abl inhibits cell extrusion during tissue folding via direct regulation of Ena function and/or localization or indirectly via regulation of polarity or junctional components will be of interest for understanding how Abl regulates epithelial integrity and polarity.

MATERIALS AND METHODS

Fly stocks

UAS-β-*gal-shRNA* (*control-shRNA*) and UAS-*abl-shRNA* expression were driven by the following maternal driver lines: [Mat67, Utr::green fluorescent protein (GFP)] (Rauzi *et al.*, 2013), [Mat67, sqh::GFP; Mat15, Gap43::CHFP], [Mat67, utr::GFP; Mat15, sqh::CHFP], [Mat67, ubi-GFP::ROCK] (Bardet *et al.*, 2013), [Mat67, Histone::GFP], [Mat67, Ecad(knock in)::GFP] (Huang *et al.*, 2009), and [Mat67, UAS-GFP::Bazooka] (Benton and St Johnston, 2003). To image abl^4 mutants and control (ctl) embryos, germline clones were generated using the FLP-DFS technique by heat shocking mutant/OvoD larvae for 2 h at 37°C for 3–4 d (Chou and Perrimon, 1992). For abl^4 mutants, [yw,hsflp; FRT^{2A}, OvoD/abl^4, FRT^{2A}] embryos were imaged (Supplemental Figure S1B). For ctl, [yw,hsflp; abl^4, FRT^{2A}/ TM3] embryos were imaged (Supplemental Figure S1B). To image the abl^4 germline live (Supplemental Figure S1, C–E), utr::GFP (F-actin) was balanced on the second chromosome of abl^4 mutant embryos [utr::GFP/Cyo; abl^4, FRT^{2A}/TM3], and germline clones were generated.

Making dsRNA

The following primers were used to generate ~500–base pair fragments of each gene of interest: **β-cat** (as described and shown to deplete β-*cat* in Tamada *et al.*, 2012), β-cat forward, 5′-TAA TAC

GAC TCA CTA TAG GGA GAC CAC CAA GAA GCG GCT ATC CAT AGA GC-3′, and β-cat reverse, 5′-TAA TAC GAC TCA CTA TAG GGA GAC CAC CAA TCG GTA TCG TAC CAG GCA GC-3′; and **Ena** (as described and shown to deplete Ena in Kiger *et al.*, 2003), Ena forward, 5′-TAA TAC GAC TCA CTA TAG GGG CCG CCT TTC CTT TGA TT-3′, and Ena reverse, 5′-TAA TAC GAC TCA CTA TAG GGC GAG CCG AGG ATG TTC TAT T-3′. Each primer contains a T7 sequence (TAA TAC GAC TCA CTA TAG GG) at its 5′-end. dsRNA was made using the MEGAscript T7 transcription kit (Ambion, Austin, TX) and resuspended in injection buffer (0.1× phosphate-buffered saline [PBS] in RNase-free water).

dsRNA injections

Embryos were dechorionated, mounted ventral side up, and then desiccated for 5 min (Drierite, Drierite Company, Salt Lake City, UT). A 3:1 halocarbon 700/halocarbon 27 oil was added on the embryo for injection. The 0–30-min-old embryos (before pole cell formation) were injected laterally with a drop size of ~40 μm, with estimated a 1:200–1:300 dilution for the dsRNA. *ena-dsRNA* and β-*cat–dsRNA* were injected into embryos at 2 μg/μl and 1.5 ng/μl, respectively. For buffer-only control, 0.1× PBS was injected.

Microscope image acquisition

Live and fixed images were acquired on a Zeiss LSM 710 confocal microscope with a 40×/numerical aperture 1.2 Apochromat water objective (Zeiss, Jena, Germany) and argon-ion, 561-nm diode, 594-nm HeNe, and 633-nm HeNe lasers. Pinhole settings were 1–2 Airy units. For two-color live imaging, simultaneous excitation was used with band-pass filters set at 499–561 nm for GFP and 599–696 nm for CHFP. All images are representative of at least six embryos unless otherwise stated.

Live imaging. Embryos were dechorionated with 1:1 bleach/water for 2 min, washed with water, and mounted ventral side up onto a slide coated with embryo glue (double-sided tape soaked in heptane). Spacer coverslips (No. 1.5) were attached using glue, and a coverslip was attached to create a chamber so that embryos were not compressed. Halocarbon 27 oil was added to the chamber. Imaging was performed at room temperature (~23°C) on a Zeiss LSM 710 confocal microscope.

Fixed imaging. Embryos were dechorionated with 1:1 bleach and water solution for 2 min, washed with water, and then fixed in 4% paraformaldehyde in 0.1 M phosphate buffer at pH 7.4 with 50% heptane for 30 min and manually devitellinized. To visualize F-actin, embryos were then incubated with Alexa Fluor 568–conjugated phalloidin (Invitrogen, Carlsbad, CA) diluted in PBS plus 0.1% Triton X-100 (PBST) overnight (~12 h) at 4°C. Embryos were blocked with 10% bovine serum albumin (BSA) in PBST. Primary and secondary antibodies were diluted in 5% BSA in PBST. Embryos were mounted ventral side up using AquaPolymount (Polysciences). The following antibodies were used for immunofluorescence: primary, anti–E-cadherin (Dcad2, 1:25; Developmental Studies Hybridoma Bank, Iowa City, IA) and anti-Enabled (5G2, 1:100; Developmental Studies Hybridoma Bank); and secondary, Alexa Fluor 488 (1:500; Invitrogen).

Microscopy image processing

Images were processed with Photoshop CS6 (Adobe, San Jose, CA) and Fiji (http://fiji.sc/wiki/index.php/Fiji). Figures were prepared using Illustrator C6 (Adobe). A Gaussian filter (kernel = 1 pixel) was applied to images. Apical images are maximum intensity projections of multiple *z*-sections (~2–3 μm), unless otherwise noted. Subapical images are one *z*-slice, ~1–2 μm below the apical sections. Cross-sections of embryos were generated using the reslice command in Fiji.

Statistical analysis

Significance between data sets was determined using the Student's *t* test. Data sets are represented with box-and-whisker-plots. A red line indicates the median. Bottom and top boxes mark the 25th and 75th percentiles of the data set, respectively. Black dashed lines mark the lowest and highest values of the data set, respectively. Red crosses indicate outliers that are beyond 1.5 times the interquartile range of the box edges. Box plots are presented in Figures 1, G and H, 2, E, H, J, and L, 3, J and K, 4, E and F, and 5, C–H, and Supplemental Figures S1, F and G, and S2, C–E.

Microscopy image analysis

Cell extrusion was quantified by manually tracking cells leaving the epithelium, using Gap34::CHFP (membrane) or Utr::GFP (F-actin) to visualize cell outlines. To quantify cell extrusion, the ventral region and the ectoderm adjacent the ventral region (nonventral cells) were examined. For the ventral region, the average field of view was 29.4 × 9 and 25.1 × 7.5 cells for control and *abl*-depleted embryos, respectively. All visible cells within the field of view were quantified. For *ctl-shRNA* and *abl-shRNA,* 13 and 17 embryos were analyzed, respectively. For *ctl* and abl^4 mutants, three and five embryos were analyzed, respectively. For *abl-shRNA* plus buffer-only injection and *abl-shRNA* plus *ena-dsRNA* injection, six embryos per condition were analyzed. For *wild-type* plus buffer-only injection and *wild-type* plus β-*cat dsRNA* injection, four embryos per condition were analyzed. The number of extruding cells during tissue folding per individual embryo was counted, and the number of cell extrusion events for each data set is presented in Figures 1G and 5G and Supplemental Figures S1F and S2E.

T1 transitions were quantified by manually tracking the reorientation of cell–cell contacts along the dorsoventral axis to the anteroposterior axis using Gap34::CHFP (membrane) or Utr::GFP (F-actin) to visualize the cell outlines. For *ctl-shRNA* and *abl-shRNA,* 13 and 17 embryos were analyzed, respectively. For *ctl* and abl^4 mutants, three and five embryos were analyzed, respectively. For *abl-shRNA* plus buffer-only injection and *abl-shRNA* plus *ena-dsRNA* injection, six embryos per condition were analyzed. For *wild-type* plus buffer-only injection and *wild-type* plus β-*cat dsRNA* injection, four embryos were analyzed. Number of T1 transitions during tissue folding is presented in Figures 1H and 5H and Supplemental Figures S1G and Figure S2D.

Cell crowding was assessed by manually counting the number of cells within a 35 μm × 35 μm area just before onset of apical MyoII. Only embryos with normal cellularization after loss of *abl* were counted. Three regions within one embryo were counted and averaged together; for *ctl-shRNA* and *abl-shRNA,* six embryos were assessed.

Dynamic Par-3, F-actin, MyoII, and Rho kinase in the basolateral domain were identified by imaging embryos expressing indicated UAS-shRNA and GFP::Par-3 (Par-3), Utr::GFP (F-actin), Sqh::GFP (MyoII), or ubi-ROCK::GFP (ROCK) ~21 μm below the apical surface. For *ctl-shRNA,* at least five embryos were analyzed per fluorescent marker. For *abl-shRNA,* six Par-3–, eight F-actin–, nine MyoII-, and six ROCK-expressing embryos were analyzed. For *ctl* and abl^4 mutants expressing utr::GFP, three and five embryos were analyzed, respectively. Representative images are presented in Figures 2, A–D (Par-3), and 3, A, B, and I, Supplemental Figure S1, C and D (F-actin),

Figures 3, C, D, G, and I (MyoII), and 3, E, F, and H (ROCK). For Figure 3, G and H, the onset of apical constriction is defined by the presence of apical MyoII or ROCK accumulation. To compare embryos at the same developmental timing, embryos with invagination occurring at the poles were compared.

Basolateral MyoII and Par-3 intensity was quantified using Fiji. For each embryo, cross-sections were constructed, and 40 slices in the center of the embryo were projected. Intensities were measured below the ventral furrow region and ~40 µm away in the nonventral region. For *ctl-shRNA*, at least five embryos were analyzed per fluorescent marker. For *abl-shRNA*, six and nine embryos were analyzed for Par-3 and MyoII, respectively. For *abl-shRNA* plus buffer-only injection and *abl-shRNA* plus *ena-dsRNA* injection, at least five embryos per condition were analyzed. For *wild-type* plus buffer-only injection and *wild-type* plus β-*cat dsRNA* injection, four embryos per condition were analyzed. The ratio of MyoII intensity in the ventral versus the nonventral region is presented in Figures 3J and 5D and Supplemental Figure S2C. The ratio of Par-3 expression in the ventral versus the nonventral region is presented in Figure 2E. To compare embryos at the same developmental timing, embryos with invagination occurring at the poles were compared.

Basolateral E-cad variability. Embryos fixed and stained for E-cad were quantified using Fiji by measuring E-cad or Par-3 intensity along basolateral junctions. For *ctl-shRNA* and *abl-shRNA*, at least five embryos were analyzed, and the junctions of at least 30 cells were measured in ventral cells. The coefficient of variance (SD/mean) of basolateral E-cad intensity is presented in Figure 2, E and H.

Junctional-to-medioapical E-cad intensity. Fixed embryos stained for E-cad were quantified using Fiji by measuring E-cad expression intensity at the junctions and in the medioapical domain. For *ctl-shRNA* and *abl-shRNA*, at least six embryos were analyzed, and 50 junctional versus medioapical comparisons were made. The ratio of E-cad intensity in fixed cells is presented in Figure 3J.

Live embryos expressing E-cad(KI)::GFP (E-Cad) were analyzed with Fiji by generating kymographs of maximum intensity projections of the top eight slices (~8 µm below the apical surface) and measuring the intensity of E-cad at and between junctions (diffusely localized) at a 85-µm line scan at three locations within each kymograph. For *ctl-shRNA* and *abl-shRNA*, three embryos were analyzed, and 90 junctional versus medioapical comparisons were made. For *abl-shRNA* plus buffer-only injection and *abl-shRNA* plus *ena-dsRNA* injection, at least four embryos were analyzed, and 90 junctional versus medioapical comparisons were made per condition. The ratio between junctional and diffuse E-cad intensity in live cells is shown in Figures 3L and 5F.

Ena localization quantification

Junctional-to-medioapical Ena. Fixed embryos stained for Ena were quantified using Fiji by measuring Ena intensity at the junctions and in the medioapical domain. For *ctl-shRNA* and *abl-shRNA*, at least seven embryos were analyzed, and 50 junctional versus medioapical comparisons were made in both ventral and lateral cells. The ratio of Ena intensity in fixed cells is presented in Figure 4E.

Basolateral Ena intensity. Fixed embryos stained for Ena were quantified using Fiji by measuring Ena intensity along basolateral junctions. For *ctl-shRNA* and *abl-shRNA*, at least five embryos were analyzed, and the junctions of at least 30 cells were measured in both ventral and lateral cells. The coefficient of variance (SD/mean) of basolateral Ena intensity in fixed cells is presented in Figure 4F.

ACKNOWLEDGMENTS

We thank the Bloomington *Drosophila* Stock Center (Bloomington, IN) for fly stocks and antibodies, as well as Thomas Lecuit, Johanns Bellaiche, Mark Peifer, and Eric Wieschaus for generously providing stocks used in this study. We also thank Matthew R. Broadus, Frank Gertler, Terry Orr-Weaver, and the Martin lab for helpful comments and discussion of the manuscript. This work was supported by National Institute of General Medical Sciences Grants F32GM113425 to J.N.J. and R01GM105984 to A.C.M.

REFERENCES

Bardet P-L, Guirao B, Paoletti C, Serman F, Léopold V, Bosveld F, Goya Y, Mirouse V, Graner F, Bellaïche Y (2013). PTEN controls junction lengthening and stability during cell rearrangement in epithelial tissue. Dev Cell 25, 534–546.

Bear JE, Gertler FB (2009). Ena/VASP: towards resolving a pointed controversy at the barbed end. J Cell Sci 122, 1947–1953.

Benton R, St Johnston D (2003). A conserved oligomerization domain in drosophila Bazooka/PAR-3 is important for apical localization and epithelial polarity. Curr Biol 13, 1330–1334.

Bertet C, Sulak L, Lecuit T (2004). Myosin-dependent junction remodelling controls planar cell intercalation and axis elongation. Nature 429, 667–671.

Chou TB, Perrimon N (1992). Use of a yeast site-specific recombinase to produce female germline chimeras in Drosophila. Genetics 131, 643–653.

Clark IBN, Muha V, Klingseisen A, Leptin M, Müller H-AJ (2011). Fibroblast growth factor signalling controls successive cell behaviours during mesoderm layer formation in Drosophila. Development 138, 2705–2715.

Courtemanche N, Gifford SM, Simpson MA, Pollard TD, Koleske AJ (2015). Abl2/Abl-related gene stabilizes actin filaments, stimulates actin branching by actin-related protein 2/3 complex, and promotes actin filament severing by cofilin. J Biol Chem 290, 4038–4046.

Dudek SM, Chiang ET, Camp SM, Guo Y, Zhao J, Brown ME, Singleton PA, Wang L, Desai A, Arce FT, *et al.* (2010). Abl tyrosine kinase phosphorylates nonmuscle Myosin light chain kinase to regulate endothelial barrier function. Mol. Biol Cell 21, 4042–4056.

Fox DT, Peifer M (2007). Abelson kinase (Abl) and RhoGEF2 regulate actin organization during cell constriction in Drosophila. Development 134, 567–578.

Franke JD, Montague RA, Kiehart DP (2005). Nonmuscle myosin II generates forces that transmit tension and drive contraction in multiple tissues during dorsal closure. Curr Biol 15, 2208–2221.

Friedl P, Wolf K (2003). Tumour-cell invasion and migration: diversity and escape mechanisms. Nat Rev Cancer 3, 362–374.

Furman C, Sieminski AL, Kwiatkowski AV, Rubinson DA, Vasile E, Bronson RT, Fässler R, Gertler FB (2007). Ena/VASP is required for endothelial barrier function in vivo. J Cell Biol 179, 761–775.

Hansen SD, Mullins RD (2010). VASP is a processive actin polymerase that requires monomeric actin for barbed end association. J Cell Biol 191, 571–584.

Harris TJC, Peifer M (2004). Adherens junction-dependent and -independent steps in the establishment of epithelial cell polarity in Drosophila. J Cell Biol 167, 135–147.

Harris TJC, Peifer M (2005). The positioning and segregation of apical cues during epithelial polarity establishment in Drosophila. J Cell Biol 170, 813–823.

Hayes KE, Walk EL, Ammer AG, Kelley LC, Martin KH, Weed SA (2013). Ableson kinases negatively regulate invadopodia function and invasion in head and neck squamous cell carcinoma by inhibiting an HB-EGF autocrine loop. Oncogene 32, 4766–4777.

Henkemeyer M, West SR, Gertler FB, Hoffmann FM (1990). A novel tyrosine kinase-independent function of Drosophila abl correlates with proper subcellular localization. Cell 63, 949–960.

Huang J, Zhou W, Dong W, Watson AM, Hong Y (2009). Directed, efficient, and versatile modifications of the *Drosophila* genome by genomic engineering. Proc Natl Acad Sci USA 106, 8284–8289.

Jodoin JN, Coravos JS, Chanet S, Vasquez CG, Tworoger M, Kingston ER, Perkins LA, Perrimon N, Martin AC (2015). Stable force balance between epithelial cells arises from F-actin turnover. Dev Cell 35, 685–697.

Kiger AA, Baum B, Jones S, Jones MR, Coulson A, Echeverri C, Perrimon N (2003). A functional genomic analysis of cell morphology using RNA interference. J Biol 2, 27.
Koleske AJ, Gifford AM, Scott ML, Nee M, Bronson RT, Miczek KA, Baltimore D (1998). Essential roles for the Abl and Arg tyrosine kinases in neurulation. Neuron 21, 1259–1272.
Lecuit T, Lenne P-F, Munro E (2011). Force generation, transmission, and integration during cell and tissue morphogenesis. Annu Rev Cell Dev Biol 27, 157–184.
Leptin M (1991). twist and snail as positive and negative regulators during Drosophila mesoderm development. Genes Dev 5, 1568–1576.
Leptin M (1995). Drosophila gastrulation: from pattern formation to morphogenesis. Annu Rev Cell Dev Biol 11, 189–212.
Leptin M, Grunewald B (1990). Cell shape changes during gastrulation in Drosophila. Development 110, 73–84.
Marinari E, Mehonic A, Curran S, Gale J, Duke T, Baum B (2012). Live-cell delamination counterbalances epithelial growth to limit tissue overcrowding. Nature 484, 542–545.
Martin AC, Gelbart M, Fernandez-Gonzalez R, Kaschube M, Wieschaus EF (2010). Integration of contractile forces during tissue invagination. J Cell Biol 188, 735–749.
Martin AC, Kaschube M, Wieschaus EF (2009). Pulsed contractions of an actin-myosin network drive apical constriction. Nature 457, 495–499.
Mason FM, Tworoger M, Martin AC (2013). Apical domain polarization localizes actin-myosin activity to drive ratchet-like apical constriction. Nat Cell Biol 15, 926–936.
Onder TT, Gupta PB, Mani SA, Yang J, Lander ES, Weinberg RA (2008). Loss of E-cadherin promotes metastasis via multiple downstream transcriptional pathways. Cancer Res 68, 3645–3654.
Oudin MJ, Hughes SK, Rohani N, Moufarrej MN, Jones JG, Condeelis JS, Lauffenburger DA, Gertler FB (2016). Characterization of the expression of the pro-metastatic Mena(INV) isoform during breast tumor progression. Clin Exp Metastasis 33, 249–261.
Philippar U, Roussos ET, Oser M, Yamaguchi H, Kim HD, Giampieri S, Wang Y, Goswami S, Wyckoff JB, Lauffenburger DA, *et al*. (2008). A Mena invasion isoform potentiates EGF-induced carcinoma cell invasion and metastasis. Dev Cell 15, 813–828.
Rauzi M, Hočevar Brezavšček A, Ziherl P, Leptin M (2013). Physical models of mesoderm invagination in Drosophila embryo. Biophys J 105, 3–10.
Shamir ER, Pappalardo E, Jorgens DM, Coutinho K, Tsai W-T, Aziz K, Auer M, Tran PT, Bader JS, Ewald AJ (2014). Twist1-induced dissemination preserves epithelial identity and requires E-cadherin. J Cell Biol 204, 839–856.
Slattum GM, Rosenblatt J (2014). Tumour cell invasion: an emerging role for basal epithelial cell extrusion. Nat Rev Cancer 14, 495–501.
Tamada M, Farrell DL, Zallen JA (2012). Abl regulates planar polarized junctional dynamics through β-catenin tyrosine phosphorylation. Dev Cell 22, 309–319.
Vesuna F, van Diest P, Chen JH, Raman V (2008). Twist is a transcriptional repressor of E-cadherin gene expression in breast cancer. Biochem Biophys Res Commun 367, 235–241.
Wang C-C, Jamal L, Janes KA (2012). Normal morphogenesis of epithelial tissues and progression of epithelial tumors. Wiley Interdiscip Rev Syst Biol Med 4, 51–78.
Wu SK, Gomez GA, Michael M, Verma S, Cox HL, Lefevre JG, Parton RG, Hamilton NA, Neufeld Z, Yap AS (2014). Cortical F-actin stabilization generates apical-lateral patterns of junctional contractility that integrate cells into epithelia. Nat Cell Biol 16, 167–178.
Wu SK, Lagendijk AK, Hogan BM, Gomez GA, Yap AS (2015). Active contractility at E-cadherin junctions and its implications for cell extrusion in cancer. Cell Cycle 14, 315–322.
Xie S, Martin AC (2015). Intracellular signalling and intercellular coupling coordinate heterogeneous contractile events to facilitate tissue folding. Nat Commun 6, 7161.
Yamada KM, Cukierman E (2007). Modeling tissue morphogenesis and cancer in 3D. Cell 130, 601–610.
Zallen JA, Wieschaus E (2004). Patterned gene expression directs bipolar planar polarity in Drosophila. Dev Cell 6, 343–355.